Arctic Surface, Cloud, and Radiation Properties Based on the AVHRR Polar Pathfinder Dataset. Part II: Recent Trends

XUANJI WANG

Cooperative Institute for Meteorological Satellite Studies, University of Wisconsin—Madison, Madison, Wisconsin

JEFFREY R. KEY

Office of Research and Applications, NOAA/NESDIS, Madison, Wisconsin

(Manuscript received 1 February 2004, in final form 7 October 2004)

ABSTRACT

Over the past 20 yr, some Arctic surface and cloud properties have changed significantly. Results of an analysis of satellite data show that the Arctic has warmed and become cloudier in spring and summer but has cooled and become less cloudy in winter. The annual rate of surface temperature change is 0.057°C for the Arctic region north of 60°N. The surface broadband albedo has decreased significantly in autumn, especially over the Arctic Ocean, indicating a later freeze-up and snowfall. The surface albedo has decreased at an annual rate of −0.15% (absolute). Cloud fraction has decreased at an annual rate of −0.6% (absolute) in winter and increased at annual rates of 0.32% and 0.16% in spring and summer, respectively. On an annual time scale, there is no trend in cloud fraction. During spring and summer, changes in sea ice albedo that result from surface warming tend to modulate the radiative effect of increasing cloud cover. On an annual time scale, the all-wave cloud forcing at the surface has decreased at an annual rate of –0.335 W m^{-2}, indicating an increased cooling by clouds. There are large correlations between surface temperature anomalies and climate indices such as the Arctic Oscillation (AO) index for some areas, implying linkages between global climate change and Arctic climate change.

1. Introduction

Recent observations have shown that the Northern Hemisphere sea ice extent and thickness have been decreasing beyond the expectation of natural climate variability (Rothrock et al. 1999; Vinnikov et al. 1999; Parkinson et al. 1999; Comiso 2002; Cavalieri et al. 2003) and that Arctic climate changes are also evident in other climate parameters such as surface air temperature, atmospheric circulation, precipitation, snowfall, biogeochemical cycling, and vegetation (Curry et al. 1996; Wallace et al. 1996; Rigor et al. 2000; Chen et al. 2002; Groves and Francis 2002a,b; Chapman and Walsh 1993; Myneni et al. 1997; Wang and Key 2003). A significant change in the climate system occurred in the late 1970s and early 1980s, as revealed in the Arctic Oscillation (AO) and other climate indices (Thompson and Wallace 1998; Thompson and Solomon 2002; Wolter and Timlin 1993; Zhang et al. 1997; Mantua et al. 1997; Wallace and Gutzler 1981). Numerous climate modeling studies have shown that the Arctic is one of the most sensitive regions to global climate change as a result of the positive feedback between surface temperature, surface albedo, and ice extent, known as the ice–albedo feedback (Manabe and Stouffer 1994; Manabe et al. 1992; Miller and Russell 2000; Meehl and Washington 1990; Curry et al. 1996). This fundamental theory has been confirmed by a variety of observational evidence, though records of Arctic climate change are brief and geographically sparse.

In this paper, we present recent Arctic climate trends in surface, cloud, and radiation properties over the period of 1982–99 based on the Advanced Very High Resolution Radiometer (AVHRR) Polar Pathfinder (APP) dataset. Possible linkages with global climate change are investigated. This paper is an extension of the work presented in Wang and Key (2003). Spatial

Corresponding author address: Dr. Xuanji Wang, Cooperative Institute for Meteorological Satellite Studies, University of Wisconsin—Madison, 1225 West Dayton Street, Madison, WI 53706.
E-mail: xuanjiw@ssec.wisc.edu

and temporal characteristics of surface, cloud, and radiation parameters are discussed in the first part of this two-part paper (Wang and Key 2005, hereafter Part I).

2. Data and analysis methods

As described in the Part I of this two-part paper, the primary dataset used in this study is a product of the APP project (Fowler et al. 2000; Meier et al. 1997). The APP dataset consists of twice-daily composites at a 5×5 km^2 pixel size over the period of 1982–99. The consistency of the products from different satellites over the period was studied by Wang and Key (2003), and they found no observable bias.

The APP dataset was extended (hereinafter APP-x) for this study to include retrievals of cloud fraction, cloud optical depth, cloud particle phase and size, cloud-top pressure and temperature, surface skin temperature, surface broadband albedo, and radiation fluxes as well as cloud radiative effects ("cloud forcing") under all-sky conditions. For computational considerations, the original 5-km APP data were subsampled to 25 km. Retrievals were done with the Cloud and Surface Parameter Retrieval (CASPR) system (Key 2002; Key et al. 2001). Radiation fluxes were calculated in CASPR using FluxNet (Key and Schweiger 1998). Atmospheric profiles of temperature and humidity from the National Centers for Environmental Prediction–National Center for Atmospheric Research (NCEP–NCAR) reanalysis dataset provided by the National Oceanic and Atmospheric Administration–Cooperative Institute for Research in Environmental Sciences (NOAA–CIRES) Climate Diagnostics Center in Boulder, Colorado, and the International Satellite Cloud Climatology Project (ISCCP) Climatological Summary Project (D2) ozone data (Rossow et al. 1996) provided by the National Aeronautics and Space Administration (NASA) Langley Research Center were also utilized in the retrievals.

The extended products have been validated with the data collected during the Surface Heat Balance of the Arctic Ocean (SHEBA) field experiment in the western Arctic (Maslanik et al. 2001; Stroeve et al. 2001; Key and Intrieri 2000) and with data from two Antarctic meteorological stations: South Pole and Neumayer (Pavolonis and Key 2003). The uncertainties of the satellite-retrieved surface, cloud, and radiation properties were discussed in the Part I of this two-part paper.

Trend analyses of the seasonal and interannual variability of cloud properties, surface properties, and radiation components were performed using least square fit regression with the full 18 yr of satellite-retrieved products in the APP-x dataset, 1982–99, in the form of

$$Y = \beta_0 + \beta_1 X, \tag{1}$$

where Y is the dependent variable such as surface skin temperature; X is the independent variable, that is, time in this study; β_0 is the intercept; and β_1 is the slope. For each parameter trend, a standard F test was performed, and confidence level was calculated to determine at what confidence level the trend is statistically significant. The F-test value can be computed by the following equation:

$$F = \frac{(\mathrm{SSY} - \mathrm{SSE})/k}{\mathrm{SSE}/(n - k - 1)}, \tag{2}$$

where $\mathrm{SSY} = \Sigma_{i=1}^{n}(Y_i - \overline{Y})^2$ and $\mathrm{SSE} = \Sigma_{i=1}^{n}(Y_i - \hat{Y}_i)^2$ are the total and error sums of squares, respectively; $\overline{Y}$ is the sample mean of the dependent variable Y; $\hat{Y}$ is the regressed or predicted values from Eq. (1) for all of Y; n is the sample size; and k is the number of independent variables (one in this study). Unless noted otherwise, all trends reported here are significant at a confidence level of 90% or higher. Each of the Arctic climate parameters was regressed with the year as the independent variable, and the trend value is the slope of the regression line along with a standard deviation of the slope. In addition to the entire Arctic region, the Arctic Ocean north of 60°N was also divided into 12 subregions as shown in Fig. 1, where the subregions are named and indicated by the numbers in the parentheses (after Thomas and Rothrock 1993; Groves and Francis 2002a,b). Two other Arctic Ocean divisions were also used for the larger ocean regions. One follows Groves and Francis (2002a,b): Pacific sector (regions 1–4), eastern/central (region 5–7), Arctic basin (regions 1–7), Atlantic sector (regions 8–9), and Greenland–Iceland–Norwegian (GIN) Seas (region 9). The other is from Serreze and Barry (2000), who divided the Arctic Ocean into three larger regions: central Arctic Ocean (CAO), Arctic Ocean, and Polar Cap as shown in Fig. 2. The Arctic landmasses north of 60°N were divided into six subregions as shown in Fig. 1: North Europe (region 13), north-central Russia (region 14), northeastern Russia (region 15), Alaska region (region 16), north Canada (region 17), and Greenland (region 18).

3. Trends in surface skin temperature and broadband albedo

Trends in surface skin temperature and broadband albedo over the period 1982–99 have been calculated for each 25-km resolution pixel within the Arctic region. Figure 3 shows the trends in surface temperature and broadband albedo for four seasons and the annual mean over the entire Arctic region north of 60°N.

The surface temperature has decreased slightly, at an

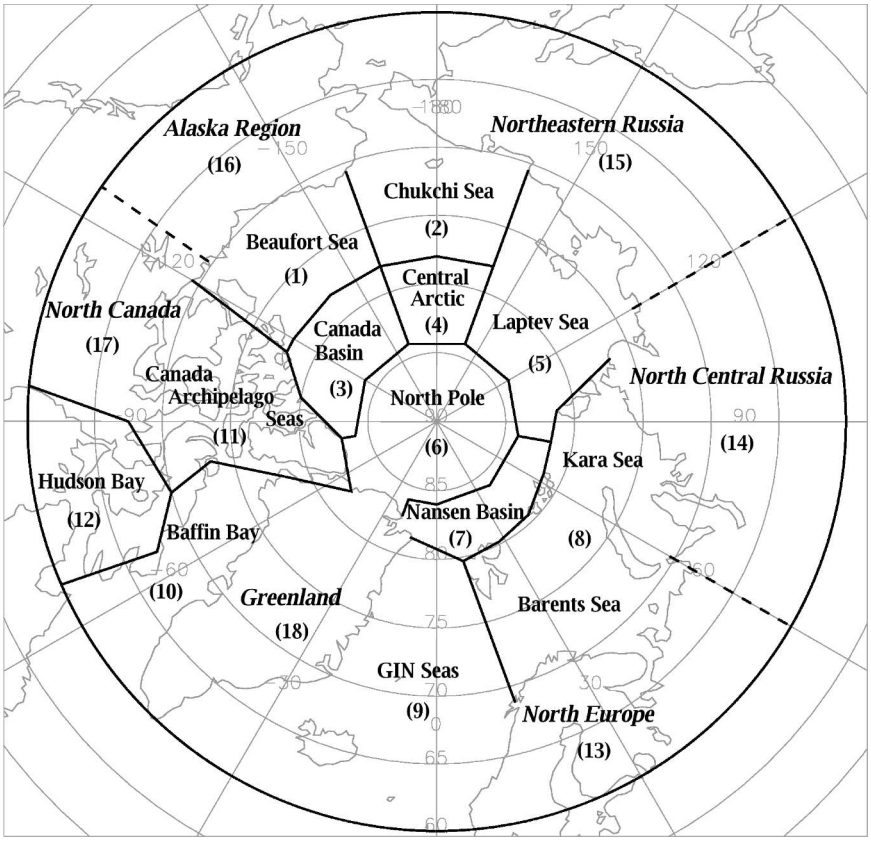

FIG. 1. Regional division of the Arctic region north of 60°N.

annual rate of –0.035°C in winter (December–February, where December data are from the previous year) with a confidence level of only 69%. Figure 4 indicates that the Arctic has experienced a cooling trend in winter around the central and eastern Arctic Ocean. This study is consistent with the recent work of Serreze et al. (2000), which showed a cooling trend in the northern North Atlantic. For the area north of 80°N, the surface temperature has decreased at –0.22°C yr^{-1} at a confidence level of as high as 99.7% in winter with a standard deviation of 0.07°C. During spring, summer, and autumn, the surface temperatures have increased at annual rates of 0.116°, 0.072°, and 0.074°C, respectively.

The surface broadband albedo in winter has decreased at an annual rate of –0.19%, but given that a large part of the Arctic region is dark throughout winter and therefore excluded from the albedo calculation, the albedo trend only represents areas between 60°N and approximately 76°N. The surface albedo has decreased at an annual rate of –0.31% in autumn, indicating later freeze-up and snowfall (Overland et al. 2002). Figure 5 shows the spatial distribution of the surface albedo trend in autumn, indicating large decreasing trends over the central and eastern Arctic Ocean and the Beaufort and Chukchi Seas. This agrees with trends in sea ice thickness and snow cover reported by other researchers (Rothrock et al. 1999; Johannessen et al. 1999; Vinnikov et al. 1999; Rignot and Thomas 2002; Anderson and Drobot 2001; Cavalieri et al. 2003). If the landmasses are excluded, the entire Arctic Ocean shows a strong warming trend, and the surface albedo has decreased both in summer and autumn. Table 1 shows the annual trends of the 18 climate parameters for some Arctic regions.

For the entire Arctic region, the annual trend in surface temperature is dominated by spring and summer trends, exhibiting warming at an annual rate of 0.057°C (average of four seasons) with a standard deviation of 0.023°C, and the annual mean surface albedo has decreased at an annual rate of −0.14% with a standard deviation of 0.08%.

4. Trends in cloud properties

a. Cloud fraction and precipitable water

Figure 6 shows the trends in cloud fraction and precipitable water (PW) for four seasons and the annual mean over the Arctic Ocean and surrounding land-

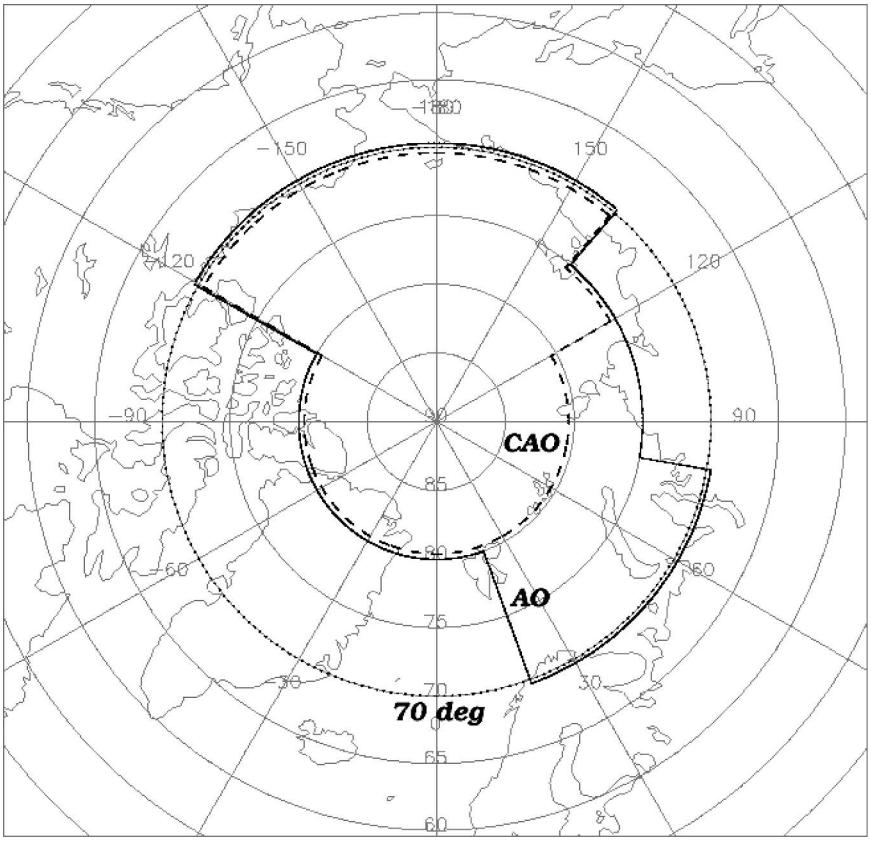

FIG. 2. Regional division of the Arctic Ocean north of 70°N from Serreze and Barry (2000): CAO (dashed), Arctic Ocean (solid; in this figure, AO denotes Artic Ocean), and Polar Cap (70°N; dotted).

masses north of 60°N. In winter, cloud cover has decreased at an annual rate of –0.60%, while in spring and summer cloud fraction has increased at annual rates of 0.32% and 0.16%, respectively. The wintertime decreasing cloudiness occurs mainly over the central Arctic Ocean north of 80°N, at an annual rate of about −1.2% with a standard deviation of 0.2%. The increasing cloudiness in spring has occurred primarily in north Canada, the Chukchi Sea and adjacent coastal areas, north-central Russia, Greenland, and the North Pole at an average annual rate of 0.6%. In summer a small increase of the cloud fraction is in large part contributed from north-central Russia and Greenland where the annual rate of the cloud fraction is about 0.6%. Most of the other regions do not exhibit trends. The decreasing cloudiness starts in autumn over the central Arctic region with an annual rate of about –0.6% and continues and enhances into winter. On an annual time scale, the seasonal trends cancel, resulting in no cloud fraction trend over most Arctic regions. One exception is the eastern-central Arctic Ocean north of 85°N, where an annual rate of –0.3% was found.

The increasing trends in cloud fraction in the warm season are generally consistent with an increasing trend in cyclonic activities (Serreze et al. 2000) and an increasing trend in total PW (obtained directly from the independent NCEP–NCAR reanalysis dataset). Over the Arctic Ocean north of 60°N, there is a strong decreasing trend in PW during winter at an annual rate of −0.001 cm, while during spring, summer, and autumn, PW has been increasing at annual rates of 0.0014, 0.0030, and 0.0021 cm, respectively. This is consistent with surface temperature trends and supports satellite retrievals, at least qualitatively. Overall, the annual mean PW trend is 0.0013 cm yr^{-1} with a standard deviation of 0.0007 cm over the Arctic Ocean. For the landmasses north of 60°N, decreasing trends in PW have been found for some areas, for example, north Europe, with a decreasing annual rate of –0.009 ± 0.0003 cm in spring. Otherwise, PW trends over the landmasses are weak or nonexistent.

b. Cloud particle phase, effective radius, and optical depth

Over the past two decades, some cloud bulk microphysical and optical characteristics have also changed.

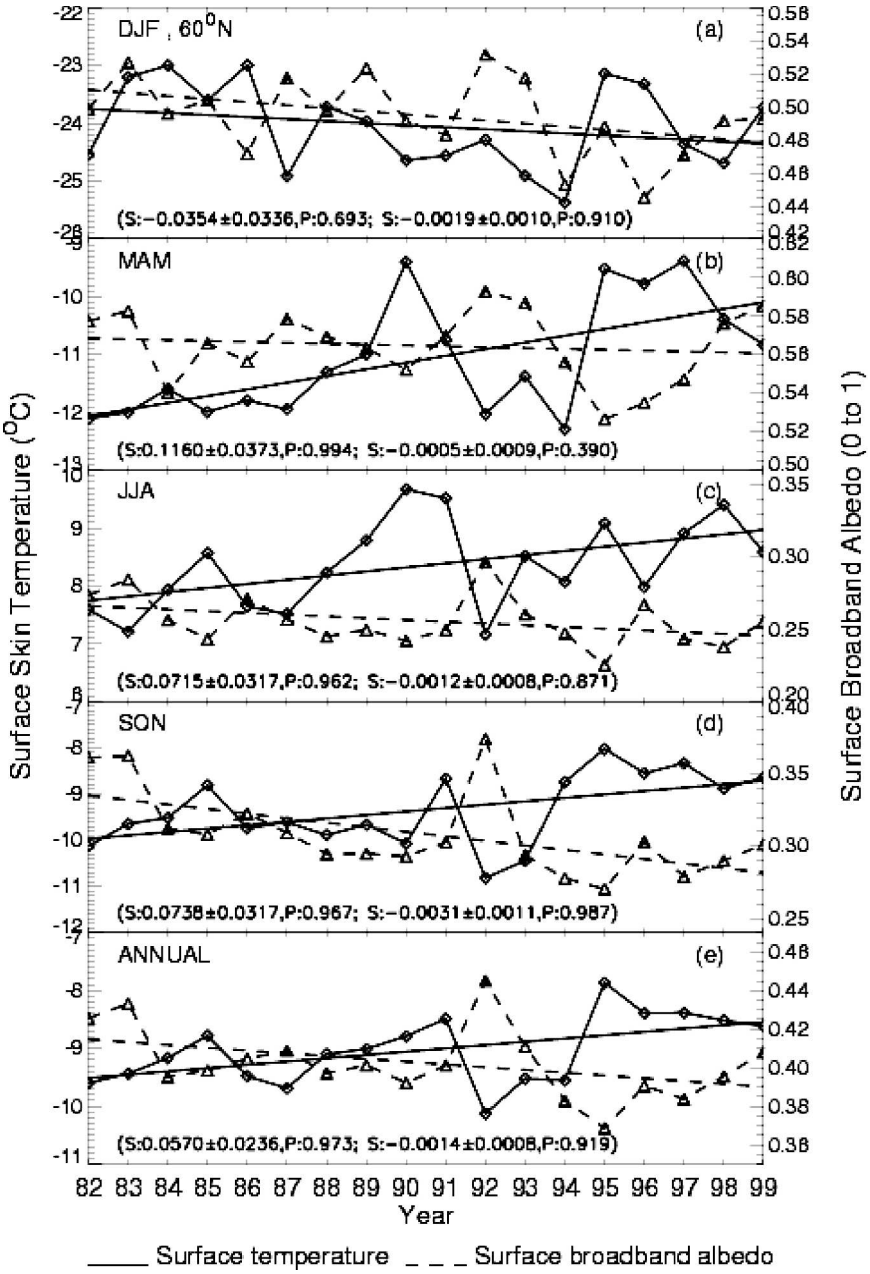

FIG. 3. Time series and trends of surface skin temperature and broadband albedo in winter [Dec–Jan–Feb (DJF)], spring [Mar–Apr–May (MAM)], summer [Jun–Jul–Aug (JJA)], and autumn [Sep–Oct–Nov (SON)] over the period of 1982–99 for the Arctic region north of 60°N. Numbers in parentheses are the trend slope per year ("*S*") with its standard deviation and the *F* test confidence level ("*P*"). The first pair of *S* and *P* denotes the surface temperature trend (solid line), and the second pair is for the surface albedo (dashed line).

Figure 7 shows the trends in cloud particle phase, effective radius, and optical depth for four seasons and the annual mean for the Arctic Ocean and surrounding landmasses north of 60°N. Cloud particle phase is indicated by two numbers: 0 for liquid phase, 1 for solid phase (ice), and a number between 0 and 1 for averages over time and/or space. A number less than 0.5 indicates that liquid-phase clouds dominate; a value greater than 0.5 indicates that ice clouds dominate. The cloud particle effective radius for liquid droplets is the ratio of the third to second moments of the drop size distribution as defined in Part I of this two-part paper. Ice

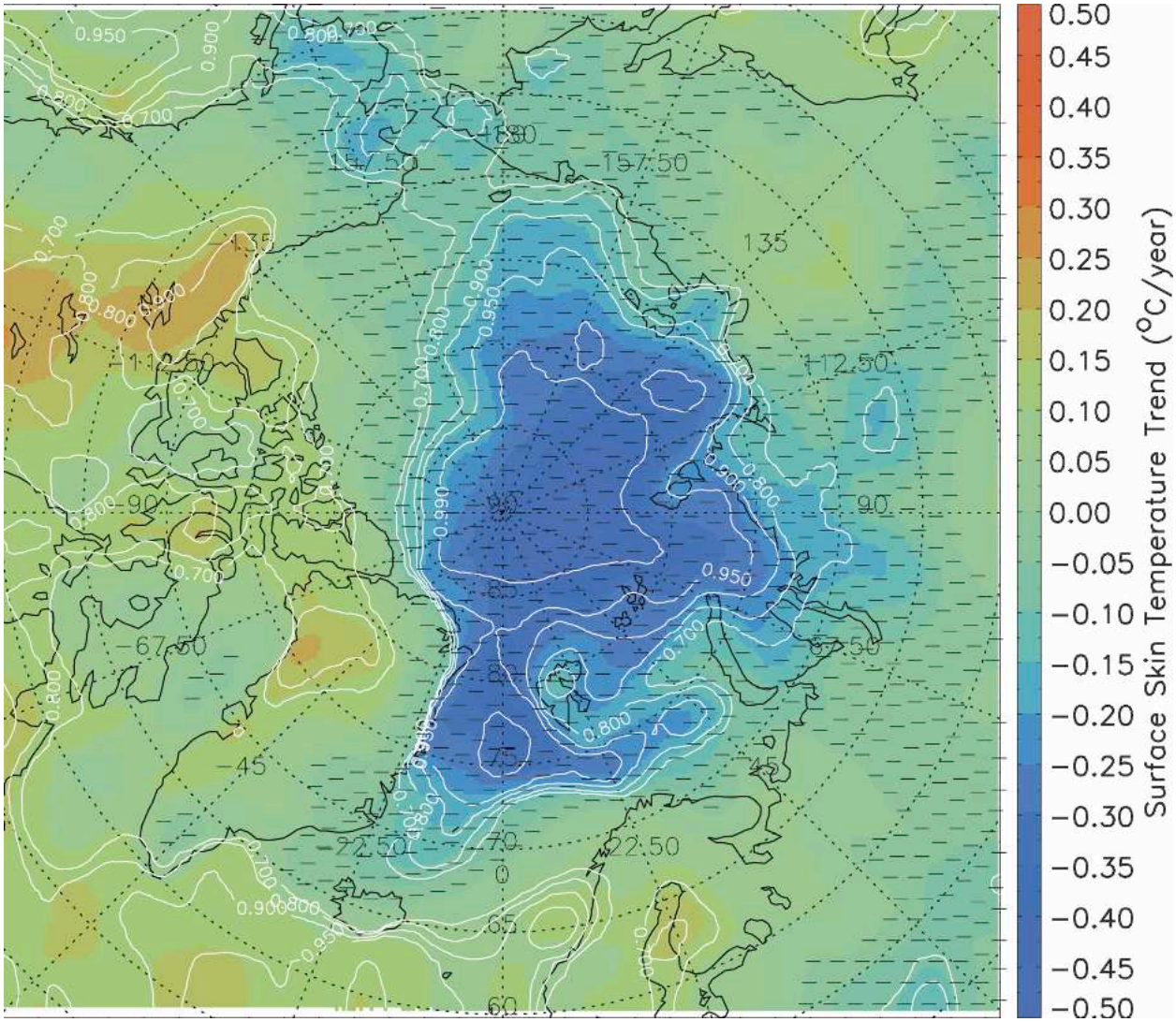

FIG. 4. Surface skin temperature trend image for the Arctic in winter over the period of 1982–99. The contours in the image stand for the confidence levels, and color represents the surface temperature trend in degrees per year as indicated by the right-side color bar. Areas with cooling trends are marked with dashes.

crystal optical properties are based on the parameterization of Key et al. (2002). The effective radius is half the effective size, as defined in Part I.

Figure 7 shows that in winter the overall cloud particle phase tends to be solid at a confidence level of only 77% (not statistically significant). Cloud particle effective radius and optical depth show no trends in winter overall in the Arctic, though some of the specific areas have trends such as at the North Pole, where there is an increasing trend in cloud particle effective radius at an annual rate of 0.5 μm in correspondence to the increasing cloud particle phase trend there.

In spring and summer clouds are increasingly in liquid phase, and the cloud particle effective radius has decreased at annual rates of –0.26 and –0.08 μm, respectively. The effective radius has decreased over all the Arctic seas except North Pole and the GIN Seas in spring. No significant trend in cloud optical depth was found in spring or summer. There is a small decreasing trend in the effective radius in summer over the western Arctic Ocean and an increasing trend in liquid-phase clouds in the GIN Seas and Barents Sea. The effective radius has a decreasing trend in autumn at an annual rate of -0.15 μm with significant areas being the Chukchi Sea, north Canada, Canada Archipelago Seas, the eastern part of Greenland, and the GIN Seas. Overall in autumn cloud phase does not show decreasing trends in the Arctic because the small increasing tendency to

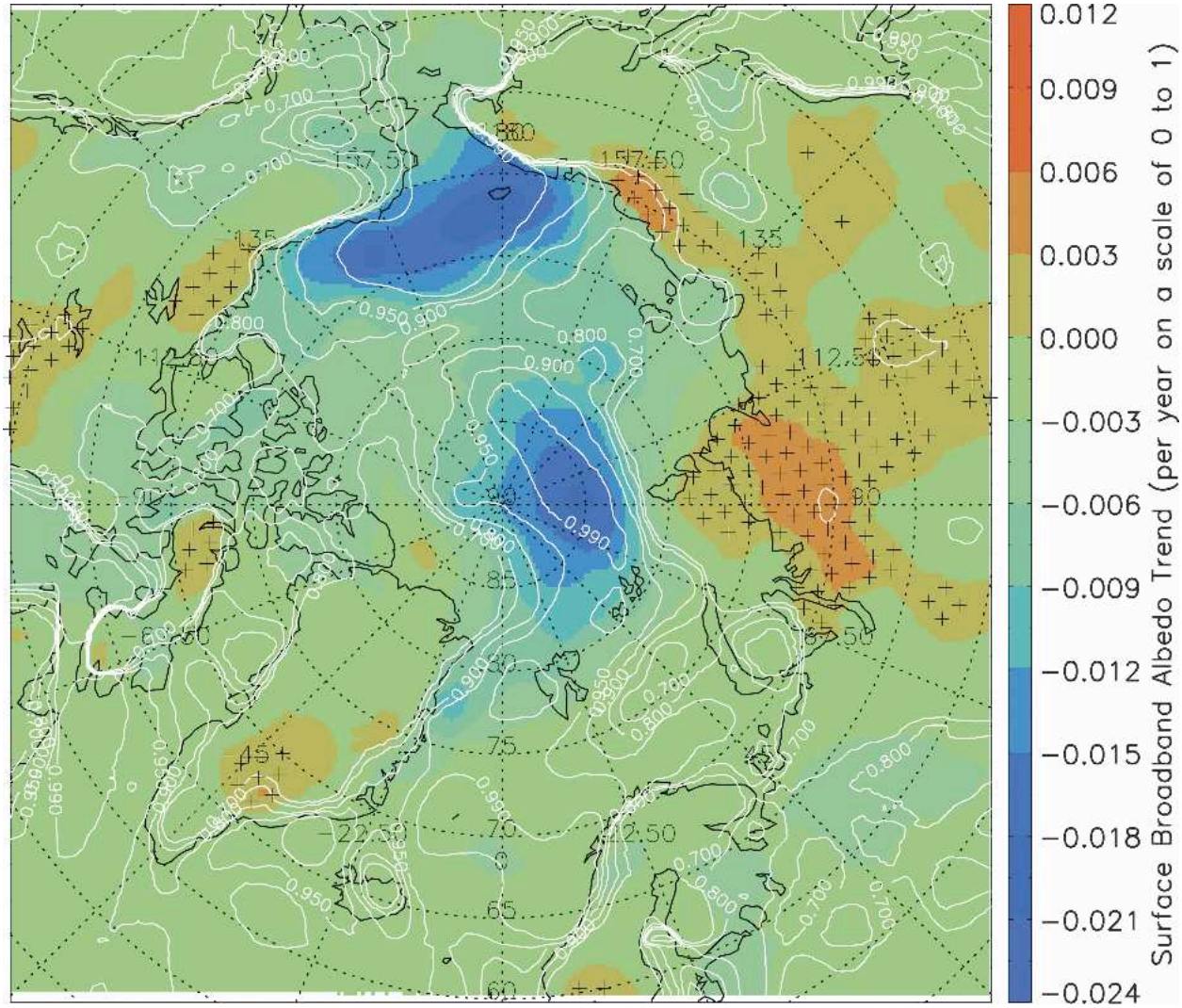

FIG. 5. Same as in Fig. 4, but for the surface albedo trend in autumn (SON). Areas with increasing trends are marked with pluses.

ice clouds in the central and eastern Arctic cancels the trend toward liquid-phase clouds elsewhere in the Arctic.

On an annual time scale, cloud particle effective radius has a decreasing rate of -0.12 μm yr^{-1} with a standard deviation of 0.027 μm, mainly over the western part of the Arctic and the Chukchi Sea, which agrees with reported tropospheric warming trends (Overland et al. 2002). Cloud particle phase and optical depth do not exhibit significant trends overall, though cloud particle phase does show a tendency toward liquid phase in the GIN Seas and north Canada.

c. Cloud-top temperature and pressure

Cloud-top temperature and pressure show some seasonal trends, but only for specific areas. Over the entire Arctic region, there are no significant trends in cloud-top temperature and pressure except in autumn when cloud-top temperature has increased at an annual rate of 0.05°C (Fig. 8).

In winter cloud-top temperature has increased in the western Arctic Ocean and north Canada, while there is a decreasing trend in cloud-top temperature in the eastern Arctic region. The spatial distribution of the cloud-top temperature trend is similar to that of surface temperature, that is, warming in the east and cooling in the west. There is a decreasing trend in cloud height (increasing cloud-top pressure) in the Chukchi Sea and central Arctic.

In spring the cloud-top temperature has increased in the west Arctic but decreased in the east Arctic, primarily in north Europe (Fig. 9). No significant trends

TABLE 1. Annual trends of the 18 climate parameters for some Arctic regions.

Region PID* name and unit	Arctic region north of 60°N	Arctic Ocean north of 60°N	Arctic land north of 60°N	Greenland Island	Polar Cap north of 70°N	Arctic Ocean	CAO
T_s (°C)	0.057 ± 0.023 (97%)	0.046 ± 0.021 (95%)	0.068 ± 0.029 (97%)	0.110 ± 0.043 (98%)	0.025 ± 0.024 (69%)	−0.012 ± 0.042 (22%)	0.038 ± 0.029 (79%)
α_s (0 to 1)	−0.0015 ± 0.0007 (92%)	−0.0023 ± 0.0008 (99%)	−0.0006 ± 0.0009 (48%)	−0.0003 ± 0.001 (26%)	−0.0023 ± 0.0009 (97%)	−0.0011 ± 0.0016 (51%)	−0.0025 ± 0.0013 (93%)
R_e (μm)	−0.122 ± 0.027 (100%)	−0.117 ± 0.033 (100%)	−0.127 ± 0.022 (100%)	−0.152 ± 0.042 (100%)	−0.110 ± 0.036 (99%)	−0.093 ± 0.036 (98%)	−0.168 ± 0.048 (100%)
τ_c (unitless)	0.0004 ± 0.0109 (2.6%)	0.0012 ± 0.0115 (8.5%)	−0.0006 ± 0.0110 (4.0%)	0.0254 ± 0.0167 (85%)	0.0050 ± 0.0122 (31%)	−0.0164 ± 0.0153 (70%)	0.0260 ± 0.0199 (79%)
ϕ_c (0 = liquid, 1 = ice)	−0.0005 ± 0.0008 (50%)	−0.0009 ± 0.0008 (72%)	−0.0002 ± 0.0008 (18%)	0.0011 ± 0.0015 (53%)	0.0000 ± 0.0009 (3.5%)	−0.0014 ± 0.0011 (81%)	−0.0003 ± 0.0001 (24%)
T_c (°C)	0.0223 ± 0.0189 (75%)	0.0410 ± 0.0214 (93%)	0.0031 ± 0.0185 (13%)	0.0168 ± 0.0350 (37%)	0.0475 ± 0.0254 (92%)	−0.0182 ± 0.0229 (56%)	0.0795 ± 0.0333 (97%)
P_c (hPa)	0.0025 ± 0.2025 (1%)	0.1707 ± 0.1880 (62%)	−0.1707 ± 0.2547 (49%)	−0.0536 ± 0.3015 (14%)	0.3510 ± 0.2094 (89%)	0.0304 ± 0.3638 (35%)	0.8886 ± 0.3134 (99%)
PW (cm)	0.0007 ± 0.0008 (63%)	0.0013 ± 0.0007 (89%)	0.0000 ± 0.0009 (8.4%)	0.0006 ± 0.0007 (64%)	0.0013 ± 0.0008 (84%)	−0.0011 ± 0.00144 (55%)	0.0023 ± 0.0011 (75%)
$SW\downarrow_{srf}$ (W m^{-2})	−0.304 ± 0.150 (94%)	−0.347 ± 0.156 (96%)	−0.259 ± 0.193 (80%)	−0.620 ± 0.340 (91%)	−0.324 ± 0.179 (91%)	−0.585 ± 0.388 (85%)	−0.311 ± 0.318 (66%)
$LW\downarrow_{srf}$ (W m^{-2})	0.182 ± 0.109 (87%)	0.140 ± 0.104 (80%)	0.227 ± 0.131 (90%)	0.363 ± 0.216 (89%)	0.014 ± 0.133 (8.3%)	0.109 ± 0.200 (41%)	−0.037 ± 0.203 (14%)
$SW\uparrow_{srf}$ (W m^{-2})	−0.357 ± 0.184 (93%)	−0.477 ± 0.156 (99%)	−0.232 ± 0.248 (64%)	−0.580 ± 0.472 (76%)	−0.401 ± 0.193 (95%)	−0.260 ± 0.371 (51%)	−0.514 ± 0.316 (88%)
$LW\uparrow_{srf}$ (W m^{-2})	0.258 ± 0.099 (98%)	0.200 ± 0.089 (96%)	0.319 ± 0.126 (98%)	0.385 ± 0.155 (98%)	0.102 ± 0.099 (68%)	0.016 ± 0.187 (6.7%)	0.125 ± 0.117 (68%)
$SW\downarrow_{toa}$ (W m^{-2})	0.014 ± 0.114 (10%)	0.016 ± 0.111 (11%)	0.012 ± 0.117 (8.3%)	0.020 ± 0.113 (14%)	0.019 ± 0.111 (14%)	0.032 ± 0.120 (21%)	0.013 ± 0.108 (10%)
$SW\uparrow_{toa}$ (W m^{-2})	0.046 ± 0.217 (17%)	−0.105 ± 0.207 (38%)	0.203 ± 0.244 (58%)	0.012 ± 0.355 (2.6%)	−0.048 ± 0.198 (19%)	0.333 ± 0.372 (62%)	−0.128 ± 0.236 (40%)
$LW\uparrow_{toa}$ (W m^{-2})	0.083 ± 0.034 (98%)	0.093 ± 0.039 (97%)	0.073 ± 0.038 (93%)	0.139 ± 0.070 (94%)	0.081 ± 0.049 (89%)	−0.014 ± 0.065 (16%)	0.088 ± 0.058 (85%)
CF_S (W m^{-2})	−0.321 ± 0.084 (100%)	−0.429 ± 0.108 (100%)	−0.209 ± 0.084 (98%)	−0.128 ± 0.051 (98%)	−0.357 ± 0.114 (99%)	−0.599 ± 0.348 (90%)	−0.287 ± 0.152 (92%)
CF_L (W m^{-2})	−0.014 ± 0.066 (17%)	−0.055 ± 0.063 (61%)	0.028 ± 0.077 (28%)	0.101 ± 0.144 (50%)	−0.115 ± 0.080 (83%)	0.077 ± 0.087 (61%)	−0.190 ± 0.127 (85%)
A_c (0 to 1)	−0.0009 ± 0.0009 (65%)	−0.0001 ± 0.0001 (82%)	−0.0006 ± 0.0011 (41%)	−0.0002 ± 0.0017 (8.5%)	−0.0021 ± 0.0001 (96%)	0.0009 ± 0.0009 (66%)	−0.0035 ± 0.0014 (98%)

* PID denotes the parameter identification number listed in Table 2, and a number in parentheses is the F-test confidence level for the above trend.

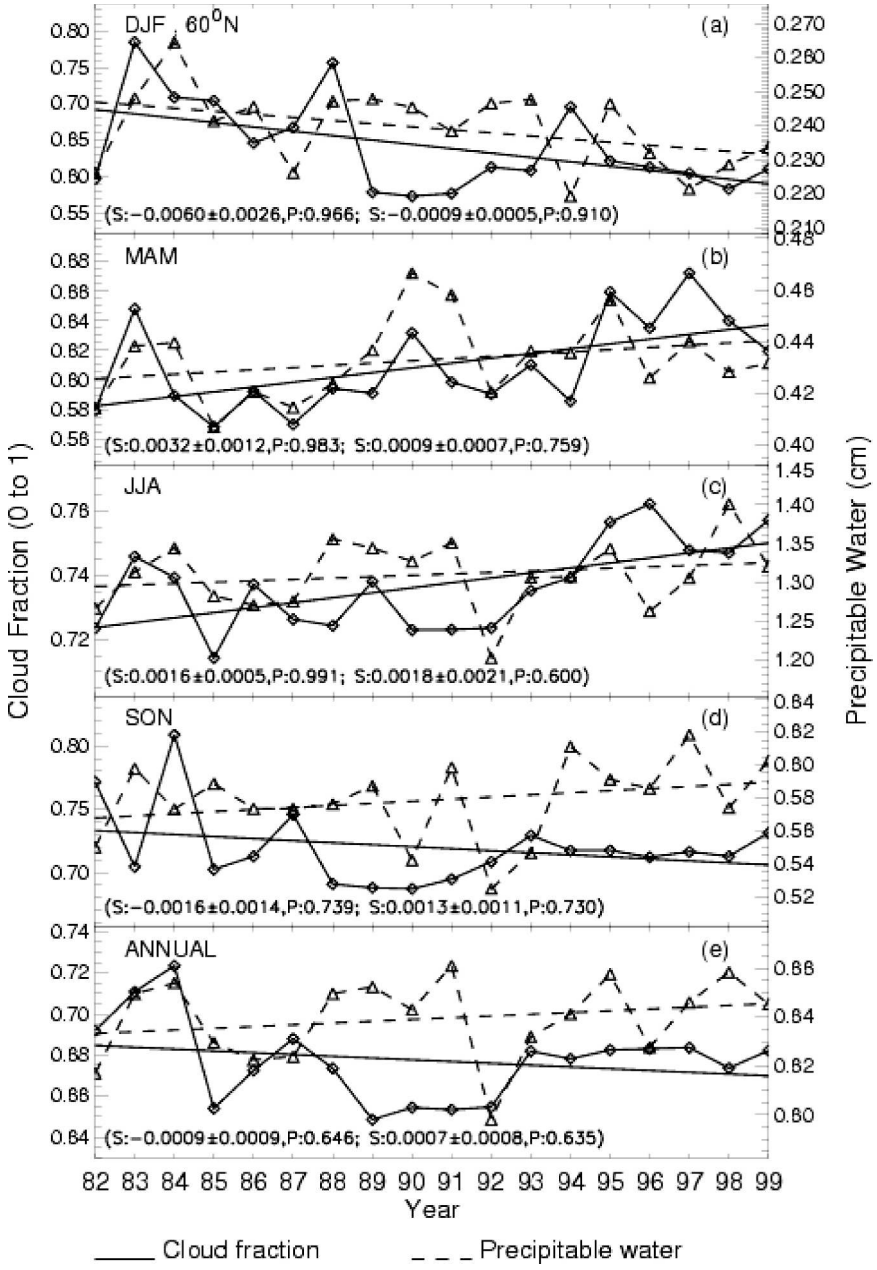

FIG. 6. Same as in Fig. 3, except that this is for the cloud fraction and PW. The first pair of *S* and *P* denotes the cloud fraction trend (solid line), and the second pair is for the PW trend (dashed line).

were found in cloud-top pressure in spring. Cloud-top temperature and pressure do not exhibit any significant trends in summer. In autumn, a strong increasing trend in cloud-top temperature was found in the western Arctic Ocean as in winter, and a decreasing trend in cloud height was found in Beaufort Sea. On an annual time scale, cloud-top temperature has an increasing trend in the west Arctic Ocean and a decreasing trend in cloud height in Beaufort Sea, indicating possibly more evaporation caused by warmer sea surface in those areas.

5. Trends in surface radiation

The radiative energy budget is a very important component of the total energy balance at the surface, con-

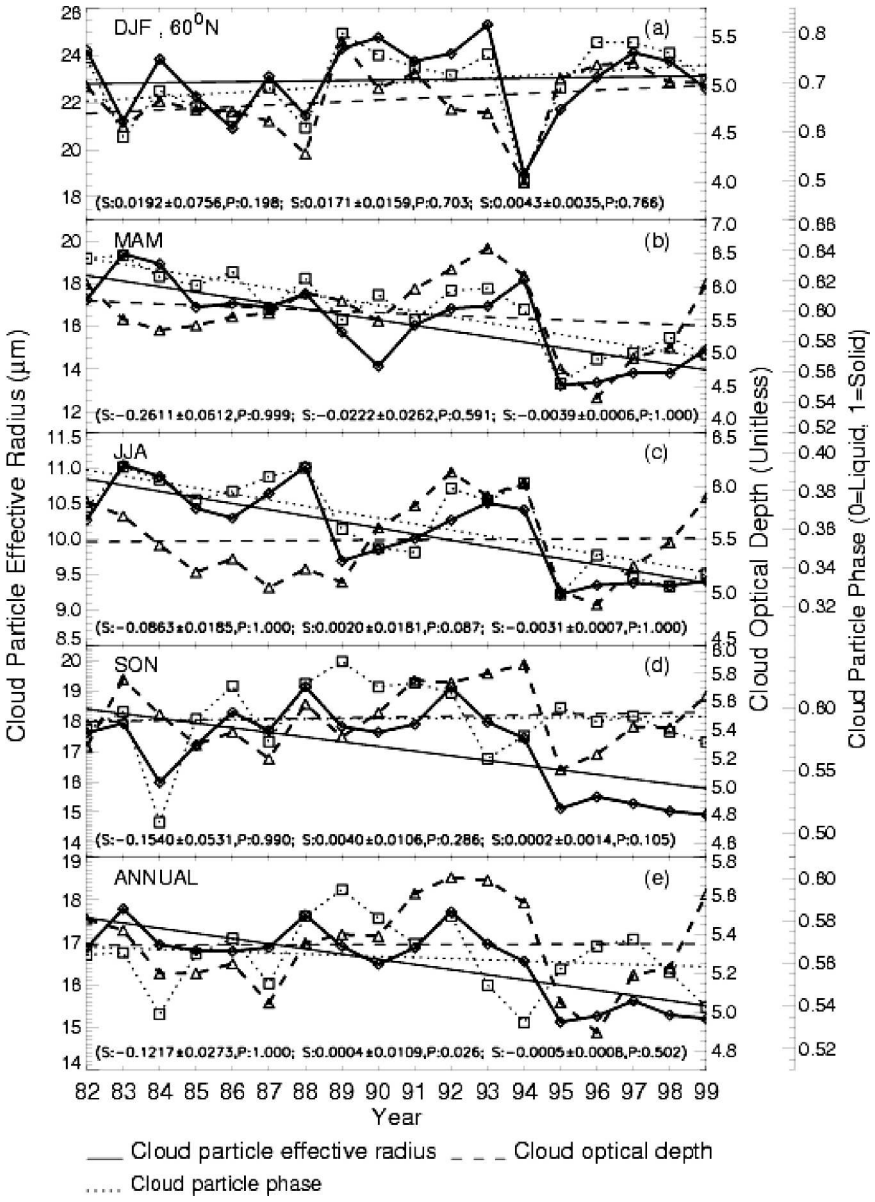

FIG. 7. Same as in Fig. 3, except that this is for the cloud particle phase, effective radius, and optical depth. The first pair of S and P denotes the cloud particle effective radius trend (solid line), the second pair is for the cloud optical depth trend (dashed line), and the third pair represents the cloud particle phase trend (dotted line).

trolling the surface temperature, sensible and latent heat capacities, and boundary layer dynamic conditions. The ice/snow–albedo feedback plays a significant role in the surface energy balance. If surface temperature increases, the ice/snow thickness and extent should decrease, and surface albedo should decrease, thus the net shortwave radiative flux at the surface should increase. Is this what happens in the real world if other climate factors like cloud fraction and precipitable water are taken into account? If, for example, cloud fraction increases, will the cloud–radiation feedback act to modulate the rise in surface temperature?

Figure 10 shows the time series and trends of the net shortwave, longwave, and all-wave radiative fluxes at the surface for four seasons and the annual mean in the Arctic region north of 60°N. The net radiative flux is defined as the downwelling minus upwelling fluxes. There are no trends in net radiation at the surface with confidence levels higher than 90% during any season. There is, however, a decreasing trend in net longwave

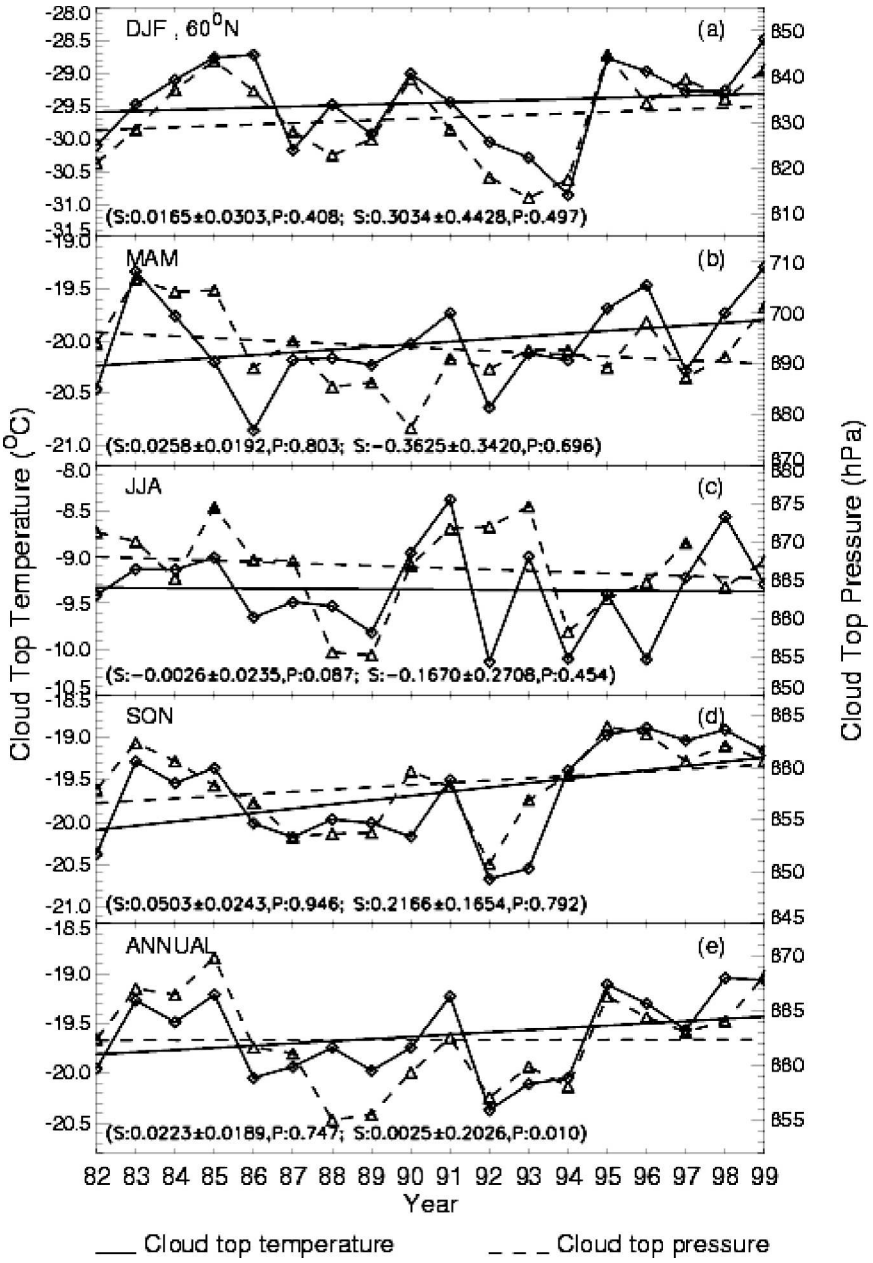

FIG. 8. Same as in Fig. 3, except that this is for the cloud-top temperature and pressure. The first pair of S and P denotes the cloud-top temperature trend (solid line), and the second pair is for the cloud-top pressure trend (dashed line).

radiative flux that has a confidence level of 98% in winter with an annual rate of –0.328 W m^{-2} due to decreasing cloud cover in the central Arctic Ocean. Given that the longwave radiative flux dominates in winter, net all-wave radiative flux has a decreasing trend at an annual rate of –0.326 W m^{-2} with a standard deviation of 0.016 W m^{-2}.

In the sunlit part of the Arctic, the net shortwave and longwave radiative fluxes tend to have opposite trends that are associated with the cloud fraction trend, that is, more clouds increase net longwave radiative flux but decrease net shortwave radiative flux at the surface by reflecting more shortwave radiation back to the atmosphere. The combined effect of clouds on net radiative flux depends on the balance of these two components. In the Beaufort Sea, for example, there are increasing trends in the net shortwave and all-wave radiative fluxes in summer and autumn primarily due to the in-

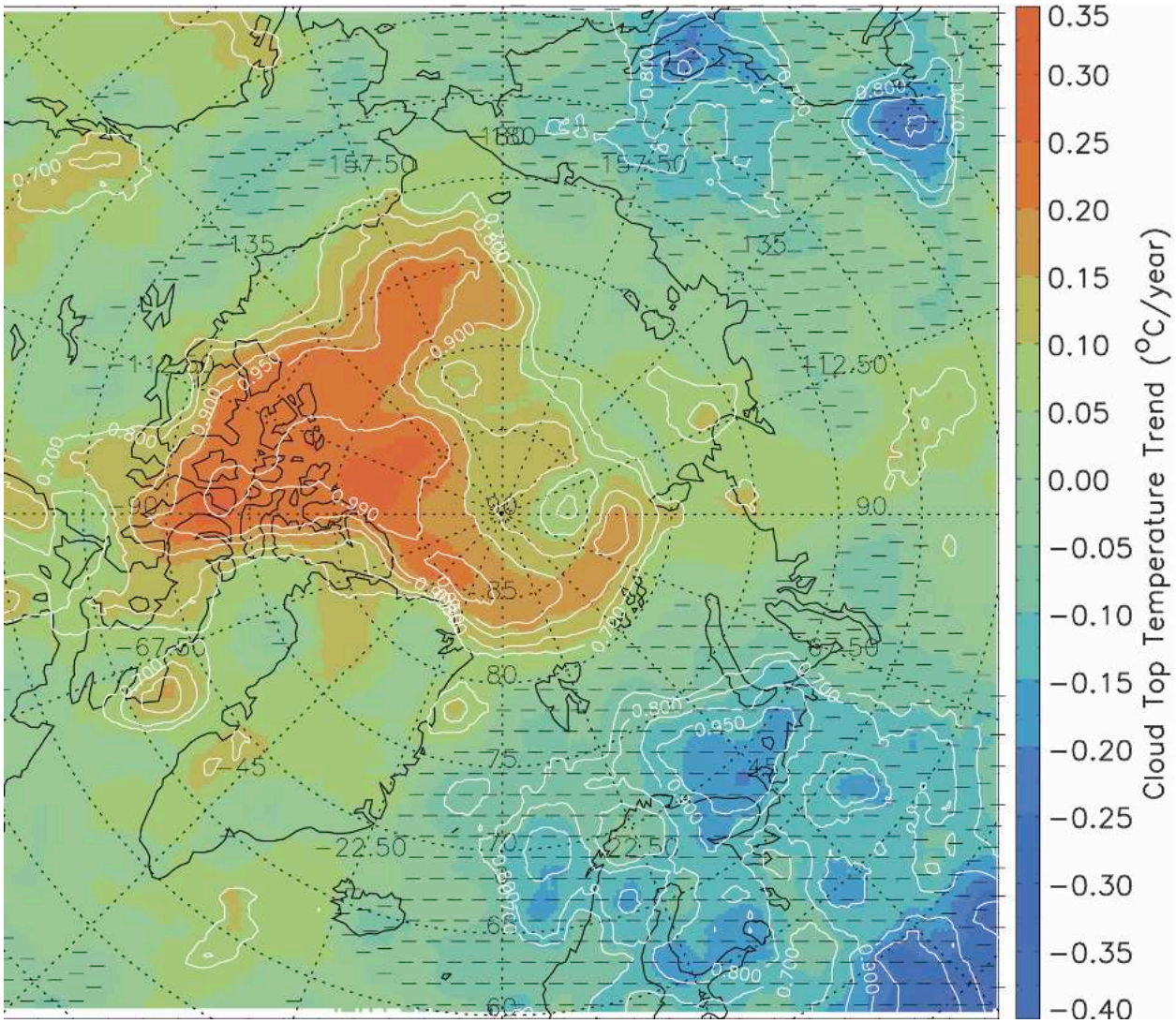

FIG. 9. Same as in Fig. 4, but for the cloud-top temperature in spring (MAM). Areas with decreasing trends are marked with dashes.

creasing trend in the surface temperature and a decreasing trend in the surface albedo. With no trend in cloud fraction there, more shortwave radiation is absorbed by the surface. Change in one surface property will not only affect other surface properties, but might also affect clouds. This implies that the cloud–radiation feedback may act to modulate net surface radiative flux.

6. Trends in cloud forcing

Cloud radiative effect, or cloud forcing, is defined as the difference between net all-sky radiative flux and net clear sky radiative flux (cf. Part I). Therefore, a positive cloud forcing indicates a warming effect and a negative value indicates a cooling effect on the surface or top of the atmosphere (TOA).

Figure 11 shows the time series and trends in shortwave, longwave, and all-wave cloud forcing for the entire Arctic. In winter the net all-wave cloud forcing, which is dominated by the longwave cloud forcing with a trend of –0.429 W m^{-2} yr^{-1}, has decreased at an annual rate of –0.475 W m^{-2} (decreasing warming effect) with a standard deviation of 0.017 W m^{-2} in response to a decreasing trend in cloud fraction (Fig. 6). A strong cooling effect by clouds can be seen in the central Arctic Ocean. The decreasing trend in the shortwave cloud forcing at an annual rate of −0.04 W m^{-2} only represents the sunlit part of the Arctic region for the latitudes lower than about 75°N.

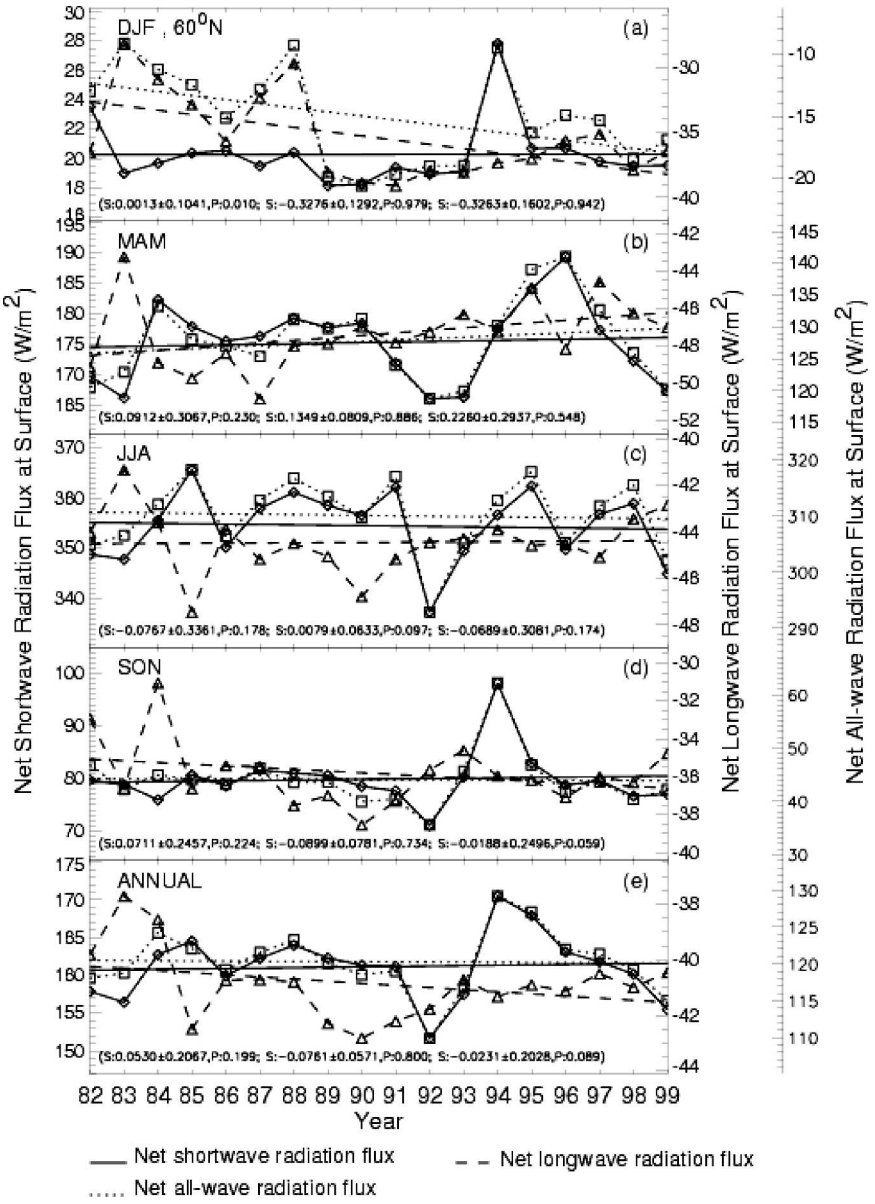

FIG. 10. Same as in Fig. 3, except that this is for the net shortwave, longwave, and all-wave radiative fluxes at the surface. The first pair of S and P denotes the net shortwave radiation trend (dotted line), the second pair is for the net longwave radiation trend (dashed line), and the third pair represents the net all-wave radiation trend (solid line).

In spring, increasing cloud fraction and warmer clouds result in a strong increasing trend in the longwave cloud forcing (greater warming) at an annual rate of 0.313 W m^{-2}, but more clouds also result in a decreasing trend in the shortwave cloud forcing (greater cooling) at an annual rate of −0.316 W m^{-2}, such that there is no significant trend in the all-wave cloud forcing.

In summer the shortwave cloud forcing is much larger in magnitude than in winter, and it dominates the net all-wave cloud forcing with an annual rate of –0.66 W m^{-2}. The longwave cloud forcing has been increasing at an annual rate of 0.113 W m^{-2}, while the net all-wave cloud forcing in summer has been decreasing at an annual rate of −0.547 W m^{-2} with a standard deviation of 0.144 W m^{-2}. The strongest cooling occurred in the Beaufort, Kara, and Barents Seas.

In autumn the cloud cooling effect on the surface is less strong than in winter and summer. The shortwave cloud forcing has decreased at an annual rate of

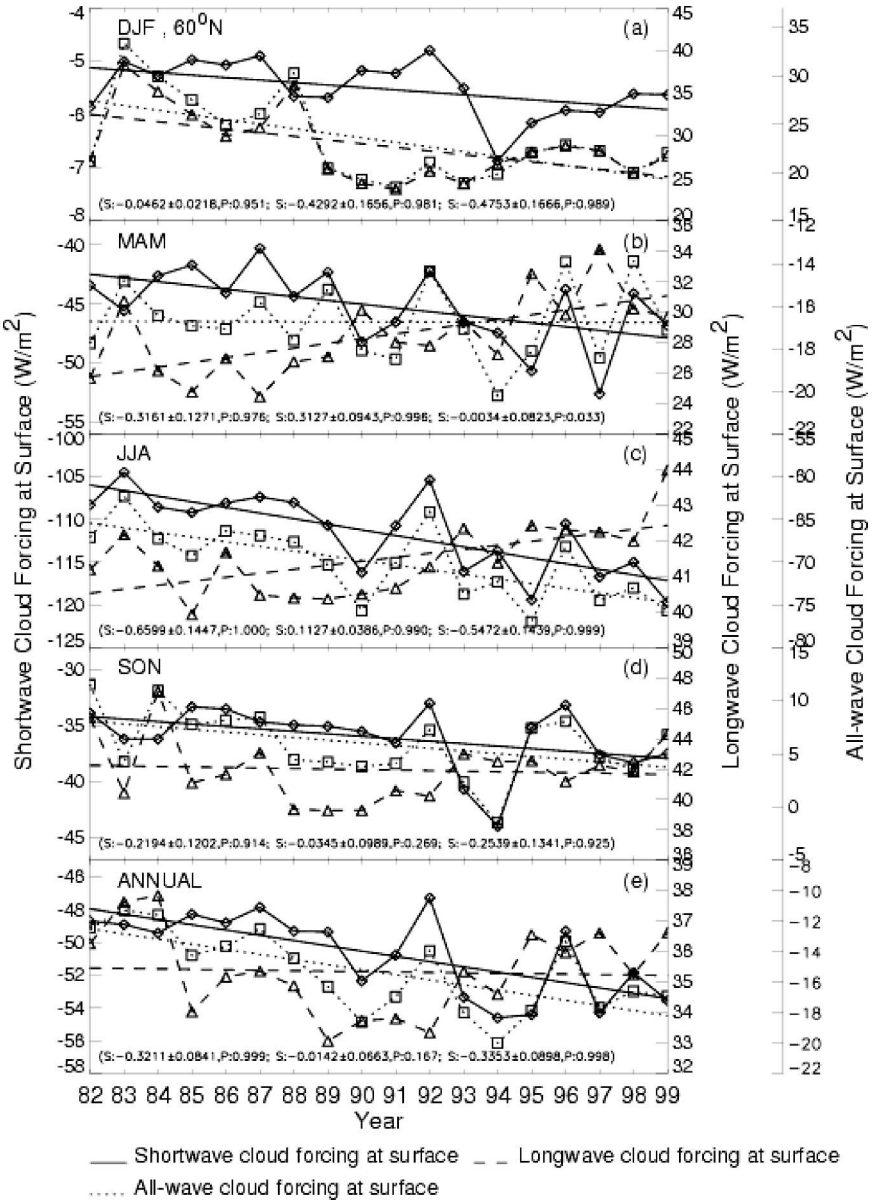

FIG. 11. Same as in Fig. 3, except that this is for the shortwave, longwave, and all-wave cloud forcing at the surface. The first pair of S and P denotes the shortwave cloud-forcing trend (dotted line), the second pair is for the longwave cloud-forcing trend (dashed line), and the third pair represents the all-wave cloud-forcing trend (solid line).

-0.22 W m^{-2}, resulting in a decreasing trend in the all-wave cloud forcing at an annual rate of –0.254 W m^{-2} and a small, statistically insignificant decreasing trend in the longwave cloud forcing.

Overall, the annual mean trend in the all-wave cloud forcing is -0.335 W m^{-2} yr^{-1} with a standard deviation of 0.089 W m^{-2}, indicating an increasing cooling effect (decreasing warming effect) by clouds. The radiative interaction between clouds, surface temperature, and surface albedo, that is, the cloud–radiation feedback, is such that there are no significant trends in the net radiation budget during winter, spring, summer, and autumn, even though there are trends in cloud and surface properties. It appears that during the sunlit part of a year, the decreases in sea ice extent and albedo that result from surface warming modulate the increasing cloud cooling effect, resulting in little or no change in the surface radiation budget.

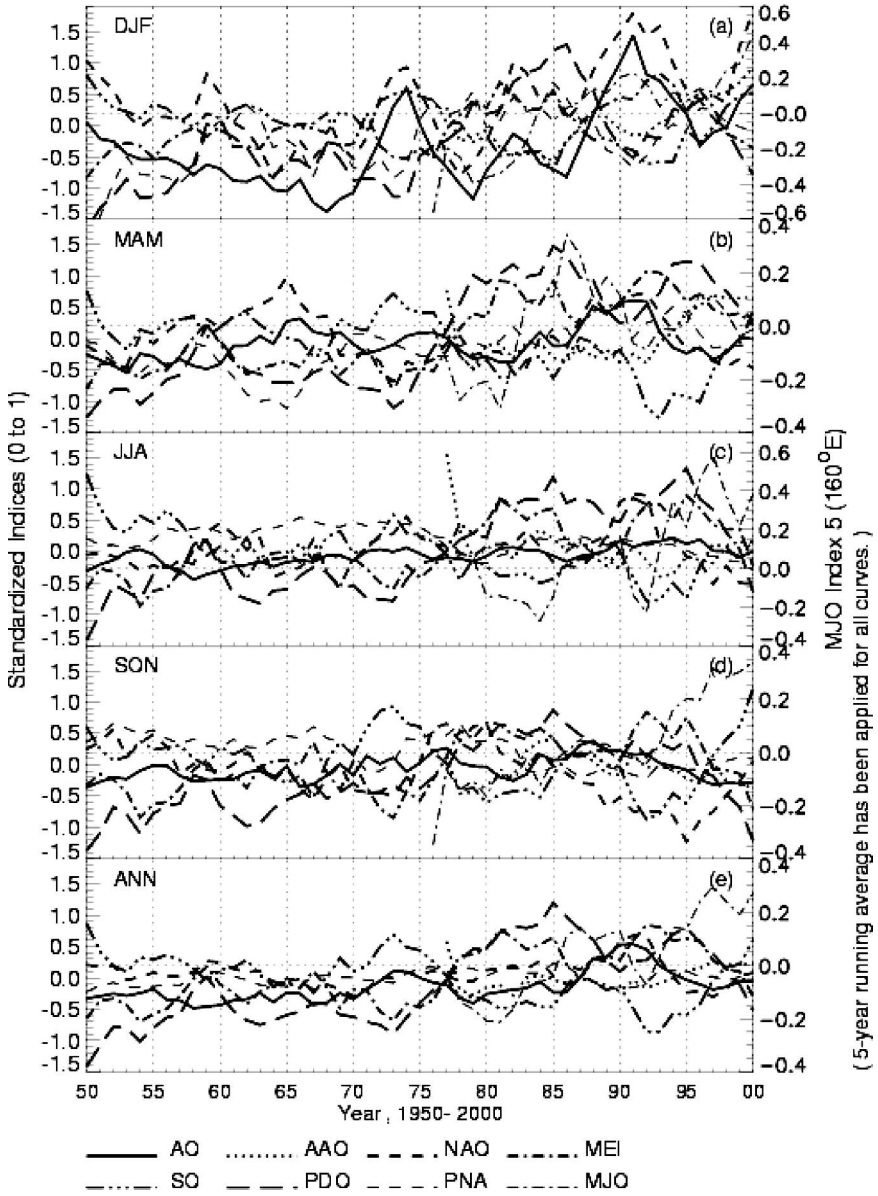

FIG. 12. Time series of the eight commonly used climate indices in winter (DJF), spring (MAM), summer (JJA), autumn (SON), and the annual mean over the period of 1950–2002.

7. Linkage between Arctic climate change and global climate change

This trend study indicates that Arctic climate change is not caused by changes in the Arctic local radiation field, as no trends in the surface radiation field were found. Therefore, interactions between the Arctic and the lower-latitude regions must play important roles in Arctic climate change. A number of climate indices have been developed to describe global, hemispheric, and regional climate patterns. The most commonly used climate indices include the AO, the North Atlantic Oscillation (NAO), the Antarctic Oscillation (AAO), the Southern Oscillation (SO), the Multivariate ENSO Index (MEI), the Pacific decadal oscillation (PDO), the Pacific–North American (PNA) pattern, and the Madden–Julian oscillation (MJO). An analysis of those climate indices shows that since the late 1970s and early 1980s the global climate has been changing rapidly, with an apparent warming trend as shown in Fig. 12. Correspondingly, Arctic climate has also been changing rapidly with profound impacts on environmental, ecological, and biological cycles. Is there any link between Arctic climate change and global climate change? What

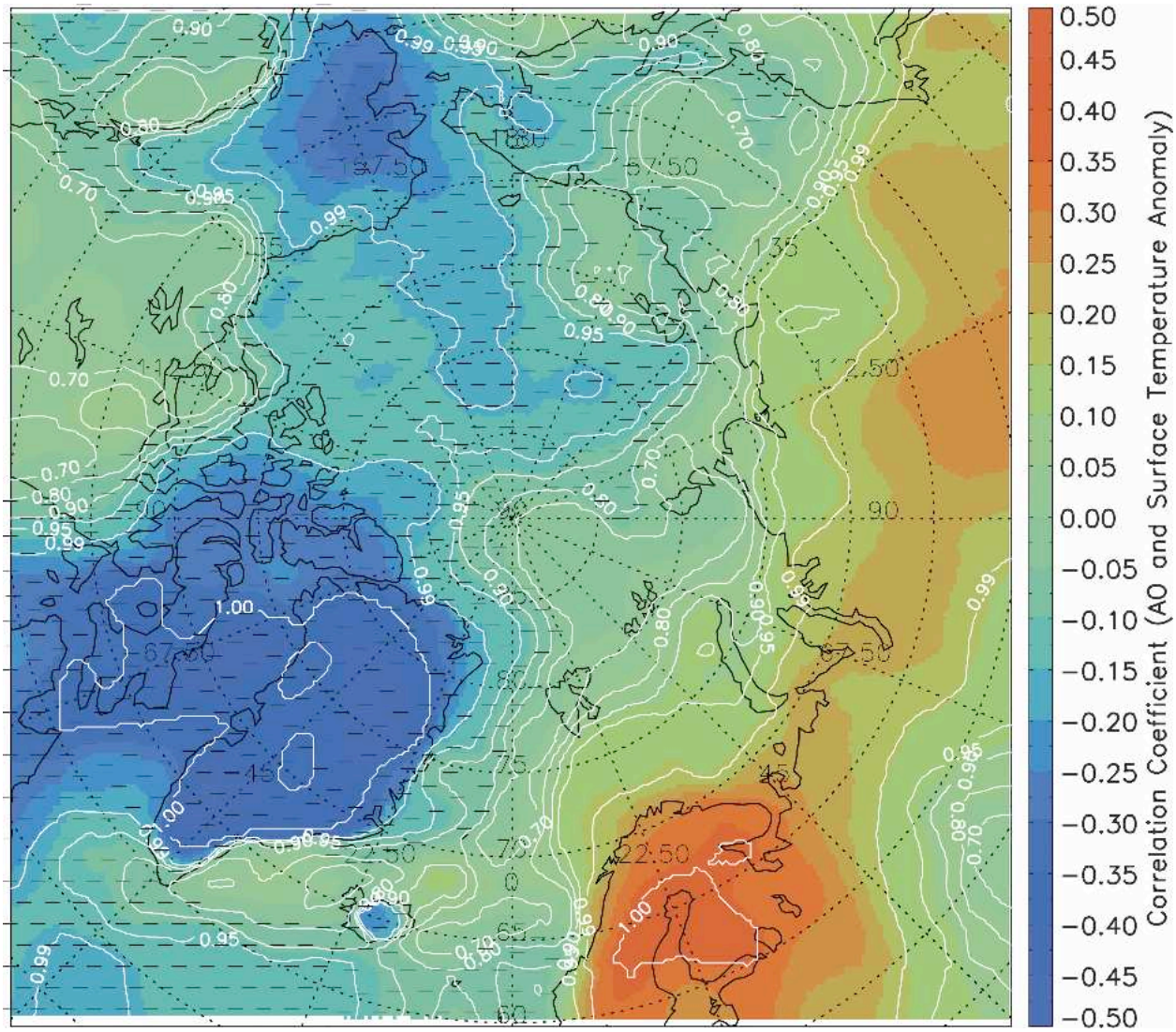

FIG. 13. Correlation coefficient image between AO indices and surface temperature anomalies from 216 monthly data during the period of 1982–99. Contours in the image stand for the confidence levels.

areas of the Arctic are most sensitive to global climate change? To answer those questions, cross-correlation coefficients between climate indices and surface skin temperature anomalies (SSTAs) were calculated for each pixel. The Student's *t* test was used to examine at what confidence level a correlation coefficient is statistically significant.

Figure 13 shows correlation coefficient image between AO indices and surface temperature anomalies from 216 months during the period of 1982–99. The contours in the image stand for the confidence levels. It clearly shows that different areas in the Arctic have different correlations with the AO. North Europe and north Russia have positive correlations with the AO, while Greenland and north Canada have negative correlations with the AO throughout all seasons except that there is positive correlation in north Canada in summer. The highest correlation occurs in winter, and the weakest correlation is in summer as expected. The AO can explain about 30% variation in surface temperature in north Europe, Baffin Bay, and Greenland in winter, and on an annual time scale it explains about 25% of the variance in surface temperature. Though the warming is prevalent in the Arctic in all seasons except winter over the central Arctic Ocean, the relationships of the AO and the surface temperature anomalies are quite different in different areas. For example, there is a positive correlation in the eastern part of the Arctic but a negative correlation in the western part of the Arctic.

Through the analyses of the relationships between Arctic surface skin temperature anomalies and climate indices, it is clear that the global climate interacts with Arctic climate. Arctic climate change is closely related to global large-scale circulation changes in both the atmosphere and ocean. Changes in the global climate seen in the climate indices can explain at least 25% of the changes in Arctic climate in every season. Table 3 lists the correlation coefficients between SSTAs and the climate indices listed above. It is clear that there are areas in the Arctic that are more sensitive to global climate change than other areas. Those areas should be very useful in monitoring and predicting Arctic climate change caused, at least in part, by global climate change.

8. Discussion and conclusions

Satellite retrievals of surface, cloud, and radiation properties over the Arctic region were used to investigate recent Arctic climate trends. Although the Arctic as a whole appears to be most sensitive to global climate change, the sign and magnitude of changes within the Arctic vary. On an annual time scale, the Arctic has been warming. Surface cooling has occurred in most of the Arctic Ocean in winter except for the Beaufort Sea, Baffin Bay, Canada Archipelago Seas, Hudson Bay, Canada Basin, and the GIN Seas, where the warming or cooling trends are not statistically significant. The strongest cooling has occurred in the Nansen Basin at an annual rate of –0.32°C. In the warm seasons (spring, summer, and autumn), all significant trends in surface skin temperature are positive. The strongest warming region is north Canada where the annual rates of the surface temperature changes are 0.140°, 0.221°, 0.145°, 0.176°, and 0.170°C for winter, spring, summer, autumn, and the annual mean, respectively.

Cloud cover has also varied over the past 20 yr, especially in winter and spring when decreasing and increasing cloud fraction trends, respectively, were found. Other cloud microphysical properties have also changed. In general, when and where the surface has cooled, clouds are more likely to be in ice phase with large cloud particle effective radius and low cloud-top temperature. Cloud optical depth does not show significant trends except for over the Beaufort Sea, where significant increasing trends have been found in winter, summer, autumn, and the annual mean, but a decreasing trend has been found in spring. In addition, cloud height has not changed significantly over most of the Arctic.

The net all-wave radiative flux at the surface only shows a significant decreasing trend in winter in the central Arctic due to the decreasing trend in cloud fraction; no trends have been found for other seasons over most of the Arctic. The radiative interaction between clouds, surface temperature, and surface albedo, that is, the cloud–radiation feedback, is such that there is no significant trend in the net radiative flux during winter, spring, summer, or autumn, even though there are trends in cloud and surface properties. It appears that during the sunlit part of a year, the decreasing trends in sea ice extent and surface albedo that result from surface warming modulate the increasing cloud cooling effect, resulting in little or no change in the surface radiation budget.

All of the commonly used climate indices indicate a significant turning point of the global climate in the late 1970s and early 1980s, along with an accelerated Arctic warming. A correlation analysis of the climate indices and surface skin temperature anomalies, cloud fraction anomalies, and precipitable water anomalies indicates that there is a linkage between Arctic climate change and global climate change. The feedback mechanisms in those areas need to be investigated with models and observations in order to determine to what degree Arctic climate change is due to local processes (e.g., evaporation) and large-scale circulation.

TABLE 2. List of the names and physical meanings of the 18 retrieved climate parameters.

PID name	Physical meaning
T_s	Surface temperature (°C or K)
α_s	Broadband albedo [range: (0, 1)]
R_e	Cloud droplet effective radius (μm)
τ_c	Cloud optical depth (unitless)
ϕ_c	Cloud particle phase (0 = liquid; 1 = ice)
T_c	Cloud-top temperature (°C or K)
P_c	Cloud-top pressure (hPa).
PW	Precipitable water (cm)
$SW\downarrow_{srf}$	Downwelling shortwave radiation at the surface (W m^{-2})
$LW\downarrow_{srf}$	Downwelling longwave radiation at the surface (W m^{-2})
$SW\uparrow_{srf}$	Upwelling shortwave radiation at the surface (W m^{-2})
$LW\uparrow_{srf}$	Upwelling longwave radiation at the surface (W m^{-2})
$SW\downarrow_{toa}$	Downwelling shortwave radiation at the TOA (W m^{-2})
$SW\uparrow_{toa}$	Upwelling shortwave radiation at the TOA (W m^{-2})
$LW\uparrow_{toa}$	Upwelling longwave radiation at the TOA (W m^{-2})
CF_S	Shortwave cloud forcing at the surface (W m^{-2})
CF_L	Longwave cloud forcing at the surface (W m^{-2})
A_c	Cloud fraction (0–1; unitless)

TABLE 3. Correlation coefficients between SSTAs and climate indices for the 18 Arctic subregions based on the 216 monthly data. Numbers in parentheses are *t*-test confidence level for the above cross-correlation coefficient. Bold type indicates correlations with confidence levels of 95% or higher.

Area name and ID No.	AO	NAO	AAO	SO	MEI	PDO	PNA
Beaufort Sea (1)	**−0.1655**	−0.1083	0.1033	0.0100	0.0268	0.0278	0.0822
	(99%)	(94%)	(94%)	(56%)	(65%)	(66%)	(89%)
Chukchi Sea (2)	**−0.1621**	**−0.1380**	−0.0921	−0.0412	0.0142	0.0201	0.0256
	(99%)	**(98%)**	(91%)	(73%)	(58%)	(62%)	(65%)
Canada Basin (3)	**−0.1758**	−0.0541	0.0375	0.0061	−0.0298	0.0022	0.0851
	(99%)	(79%)	(71%)	(54%)	(67%)	(51%)	(89%)
Central Arctic (4)	**−0.1790**	−0.0341	−0.0499	−0.0616	0.0365	0.0722	0.0738
	(99%)	(69%)	(77%)	(82%)	(70%)	(85%)	(86%)
Laptev Sea (5)	−0.0686	0.0476	−0.1045	−0.0523	−0.0013	0.0664	0.0732
	(84%)	(76%)	(94%)	(78%)	(51%)	(83%)	(86%)
North Pole (6)	−0.0973	0.1053	−0.0861	−0.0691	−0.0334	0.0458	0.0318
	(93%)	(94%)	(90%)	(84%)	(69%)	(75%)	(68%)
Nansen Basin (7)	−0.0555	**0.1633**	−0.0719	−0.0725	−0.0242	0.0212	−0.0563
	(79%)	**(99%)**	(85%)	(86%)	(64%)	(62%)	(79%)
Kara and Barents Sea (8)	**0.1521**	**0.2009**	−0.0902	−0.0287	−0.0594	−0.0234	0.0507
	(98%)	**(99%)**	(91%)	(66%)	(81%)	(63%)	(77%)
GIN Seas (9)	−0.0384	0.0821	0.0241	**0.1366**	**−0.2416**	**−0.2514**	**−0.1521**
	(71%)	(89%)	(64%)	**(98%)**	**(99%)**	**(99%)**	**(99%)**
Baffin Bay (10)	**−0.4246**	**−0.3425**	0.0909	**0.1990**	**−0.2586**	−0.0344	0.0250
	(100%)	**(100%)**	(91%)	**(99%)**	**(99%)**	(69%)	(64%)
Canada Archipelago Seas (11)	**−0.2565**	**−0.1970**	0.0649	**0.1758**	**−0.2022**	−0.0554	0.1005
	(99%)	**(99%)**	(83%)	**(99%)**	**(99%)**	(79%)	(93%)
Hudson Bay (12)	**−0.3538**	**−0.2936**	0.0607	**0.2118**	**−0.2417**	−0.0878	0.0856
	(100%)	**(100%)**	(81%)	**(99%)**	**(99%)**	(90%)	(89%)
North Europe (13)	**0.3694**	**0.1721**	−0.0827	**0.1380**	**−0.1138**	**−0.2301**	**−0.1706**
	(100%)	**(99%)**	(89%)	**(98%)**	**(95%)**	**(99%)**	**(99%)**
North-central Russia (14)	**0.2611**	**0.1838**	0.0008	−0.0913	0.0150	−0.0447	0.0475
	(99%)	**(99%)**	(50%)	(91%)	(59%)	(74%)	(76%)
Northeastern Russia (15)	0.0087	−0.0940	−0.0252	0.0997	−0.0793	−0.0405	0.0360
	(55%)	(92%)	(64%)	(93%)	(88%)	(72%)	(70%)
Alaska region (16)	**−0.2344**	−0.0946	0.0315	**−0.1507**	**0.1178**	**0.1115**	**0.4413**
	(99%)	(92%)	(68%)	**(99%)**	**(96%)**	**(95%)**	**(100%)**
North Canada (17)	**−0.1580**	−0.1009	0.0942	**0.1463**	**−0.1573**	**−0.1142**	**0.1624**
	(99%)	(93%)	(92%)	**(98%)**	**(99%)**	**(95%)**	**(99%)**
Greenland Island (18)	**−0.5226**	**−0.4894**	**0.1241**	**0.1785**	**−0.2252**	−0.0798	−0.0705
	(100%)	**(100%)**	**(97%)**	**(99%)**	**(99%)**	(88%)	(85%)

Acknowledgments. This work was supported by the National Oceanic and Atmospheric Administration (NOAA) Arctic Research Office and the National Science Foundation (NSF; Grants OPP-0240827 and OPP-0230317). We thank C. Fowler, J. Maslanik, T. Scambos, and T. Haran for their work on the AVHRR Polar Pathfinder dataset. The National Snow and Ice Data Center (NSIDC) provided the standard APP dataset. The NCEP–NCAR reanalysis global profile dataset was provided by the NOAA–CIRES Climate Diagnostics Center. The NASA Langley Research Center provided the ISCCP D2 ozone dataset. Thanks also go to the two anonymous reviewers for their helpful comments and suggestions. The views, opinions, and findings contained in this report are those of the author(s) and should not be construed as an official National Oceanic and Atmospheric Administration or U.S. Government position, policy, or decision.

REFERENCES

Anderson, M. R., and S. D. Drobot, 2001: Spatial and temporal variability in snowmelt onset over Arctic sea ice. *Ann. Glaciol.,* **33,** 74–78.

Cavalieri, D. J., C. L. Parkinson, and K. Y. Vinnikov, 2003: 30-year satellite reveals contrasting Arctic and Antarctic decadal sea ice variability. *Geophys. Res. Lett.,* **30,** 1970, doi:10.1029/2003GL018031.

Chapman, W. L., and J. E. Walsh, 1993: Recent variations of sea ice and air temperature in high latitudes. *Bull. Amer. Meteor. Soc.,* **74,** 33–47.

Chen, Y., J. A. Francis, and J. R. Miller, 2002: Surface temperature of the Arctic: Comparison of TOVS satellite retrievals with surface observations. *J. Climate,* **15,** 3698–3708.

Comiso, J. C., 2002: A rapid declining perennial sea ice cover in the Arctic. *Geophys. Res. Lett.,* **29,** 1956, doi:10.1029/2002GL015650.

Curry, J. A., W. B. Rossow, D. Randall, and J. L. Schramm, 1996: Overview of Arctic cloud and radiation characteristics. *J. Climate,* **9,** 1731–1764.

Fowler, C., J. Maslanik, T. Haran, T. Scambos, J. Key, and W. Emery, 2000: AVHRR Polar Pathfinder twice-daily 5 km EASE-grid composites. National Snow and Ice Data Center, Boulder, CO. [Available online at http://nsidc.org/data/docs/daac/nsidc0066_avhrr_5km.gd.html.]

Groves, D. G., and J. A. Francis, 2002a: Variability of the Arctic atmospheric moisture budget from TOVS satellite data. *J. Geophys. Res.,* **107,** 4785, doi:10.1029/2002JD002285.

——, and ——, 2002b: Moisture budget of the Arctic from TOVS satellite data. *J. Geophys. Res.,* **107,** 4391, doi:10.1029/2001JD001191.

Johannessen, O. M., E. V. Shalina, and M. W. Miles, 1999: Satellite evidence for an Arctic sea ice cover in transformation. *Science,* **286,** 1937–1939.

Key, J., 2002: The Cloud and Surface Parameter Retrieval (CASPR) system for polar AVHRR user's guide, Cooperative Institute for Meteorological Satellite Studies, University of Wisconsin—Madison, 68 pp. [Available online at http://stratus.ssec.wisc.edu/caspr/documentation.html.]

——, and A. J. Schweiger, 1998: Tools for atmospheric radiative transfer: Streamer and FluxNet. *Comput. Geosci.,* **24,** 443–451.

——, and J. Intrieri, 2000: Cloud particle phase determination with the AVHRR. *J. Appl. Meteor.,* **39,** 1797–1805.

——, X. Wang, J. Stoeve, and C. Fowler, 2001: Estimating the cloudy-sky albedo of sea ice and snow from space. *J. Geophys. Res.,* **106** (D12), 12 489–12 497.

——, P. Yang, B. A. Baum, and S. L. Nasin, 2002: Parameterization of shortwave ice cloud optical properties for various particle habits. *J. Geophys. Res.,* **107,** 4181, doi:10.1029/2001JD000742.

Manabe, S., and R. J. Stouffer, 1994: Multiple-century response of a coupled ocean–atmosphere model to an increase of atmospheric carbon dioxide. *J. Climate,* **7,** 5–23.

——, M. J. Spelman, and R. J. Stouffer, 1992: Transient response of a coupled ocean–atmosphere model to gradual changes of atmospheric CO_2. Part II: Seasonal response. *J. Climate,* **5,** 105–126.

Mantua, N. J., S. R. Hare, Y. Zhang, J. M. Wallace, and R. C. Francis, 1997: A Pacific decadal climate oscillation with impacts on salmon. *Bull. Amer. Meteor. Soc.,* **78,** 1069–1079.

Maslanik, J. A., J. Key, C. W. Fowler, T. Nguyen, and X. Wang, 2001: Spatial and temporal variability of satellite-derived cloud and surface characteristics during FIRE-ACE. *J. Geophys. Res.,* **106** (D14), 15 233–15 249.

Meehl, G. A., and W. M. Washington, 1990: CO_2 climate sensitivity and snow-sea-ice parameterization in an atmospheric GCM coupled to a mixed-layer ocean model. *Climate Change,* **16,** 283–306.

Meier, W., J. A. Maslanik, J. R. Key, and C. W. Fowler, 1997: Multiparameter AVHRR-derived products for Arctic climate studies. *Earth Interactions*, **1**. [Available online at http://EarthInteractions.org.]

Miller, J. R., and G. L. Russell, 2000: Projected impact of climatic change on the freshwater and salt budgets of the Arctic Ocean by a GCM. *Geophys. Res. Lett.,* **27,** 1183–1186.

Myneni, R. B., C. D. Keeling, C. J. Tucker, G. Asrar, and R. R. Nemani, 1997: Increased plant growth in the northern high latitudes from 1981 to 1991. *Nature,* **386,** 698–702.

Overland, J. E., M. Wang, and N. A. Bond, 2002: Recent temperature changes in the western Arctic during spring. *J. Climate,* **15,** 1702–1716.

Parkinson, C. L., D. J. Cavalieri, P. Gloersen, H. J. Zwally, and J. C. Comiso, 1999: Arctic sea ice extents, areas, and trends, 1978–1996. *J. Geophys. Res.,* **104** (C9), 20 837–20 856.

Pavolonis, M., and J. Key, 2003: Antarctic cloud radiative forcing at the surface estimated from the AVHRR Polar Pathfinder and ISCCP D1 datasets, 1985–1993. *J. Appl. Meteor.,* **42,** 827–840.

Rignot, E., and R. H. Thomas, 2002: Mass balance of Polar ice sheets. *Science,* **297,** 1502–1506.

Rigor, I., R. L. Colony, and S. Martin, 2000: Variations in surface air temperature observations in the Arctic, 1979–97. *J. Climate,* **13,** 896–914.

Rossow, W. B., A. Walker, D. Beuschel, and M. Roiter, 1996: International satellite cloud climatology project (ISCCP) documentation of new cloud datasets. WMO/TD 737, World Meteorological Organization, 115 pp. [Available online at: http://isccp.giss.nasa.gov/docs/documents.html.]

Rothrock, D. A., Y. Yu, and G. A. Maykut, 1999: Thinning of the Arctic sea-ice cover. *Geophys. Res. Lett.,* **26,** 3469–3472.

Serreze, M. C., and R. G. Barry, 2000: Atmospheric components of the Arctic Ocean hydrologic budget assessed from rawinsonde data. *The Fresh-Water Budget of the Arctic Ocean,* E. L. Lewis, Ed., Kluwer Academic, 141–161.

——, and Coauthors, 2000: Observational evidence of recent change in the northern high-latitude environment. *Climate Change,* **46,** 159–207.

Stroeve, J., J. Box, C. Fowler, T. Haran, and J. R. Key, 2001: Intercomparison between in situ and AVHRR Polar Pathfinder-derived surface albedo over Greenland. *Remote Sens. Environ.,* **75,** 360–374.

Thomas, D. R., and D. A. Rothrock, 1993: The Arctic Ocean balance: A Kalman smoother estimate. *J. Geophys. Res.,* **98** (C6), 10 053–10 062.

Thompson, D. W. J., and J. M. Wallace, 1998: The Arctic oscillation signature in the wintertime geopotential height and temperature fields. *Geophys. Res. Lett.,* **25,** 1297–1300.

——, and S. Solomon, 2002: Interpretation of recent Southern Hemisphere climate change. *Science,* **296,** 895–899.

Vinnikov, K. Y., and Coauthors, 1999: Global warming and northern hemisphere sea ice extent. *Science,* **286,** 1934–1937.

Wallace, J. M., and D. S. Gutzler, 1981: Teleconnections in the geopotential height field during the Northern Hemisphere winter. *Mon. Wea. Rev.,* **109,** 784–812.

——, Y. Zhang, and L. Bajuk, 1996: Interpretation of interdecadal trends in Northern Hemisphere surface air temperature. *J. Climate,* **9,** 249–259.

Wang, X. J., and J. R. Key, 2003: Recent trends in Arctic surface, cloud, and radiation properties from space. *Science,* **299,** 1725–1728.

——, and ——, 2005: Arctic surface, cloud, and radiation properties based on the AVHRR Polar Pathfinder dataset. Part I: Spatial and temporal characteristics. *J. Climate,* **18,** 2558–2574.

Wolter, K., and M. S. Timlin, 1993: Monitoring ENSO in COADS with a seasonally adjusted principal component index. *Proc. 17th Climate Diagnostics Workshop,* Norman, OK, NOAA/NMC/CAC, 52–57.

Zhang, Y., J. M. Wallace, and D. S. Battisti, 1997: ENSO-like interdecadal variability: 1900–93. *J. Climate,* **10,** 1004–1020.